ACS Sustainable Chemistry & Engineering

Research Article

pubs.acs.org/journal/ascecg

Three-Dimensional Nanoarchitecture of $BiFeO_3$ Anchored TiO_2 Nanotube Arrays for Electrochemical Energy Storage and Solar Energy Conversion

Ayan Sarkar,[†,⊥] Ashutosh K. Singh,[‡,⊥] Debasish Sarkar,[§,⊥] Gobinda Gopal Khan,[*,†,⊥] and Kalyan Mandal[‡]

[†]Centre for Research in Nanoscience and Nanotechnology, University of Calcutta, Technology Campus, Block JD2, Sector III, Salt Lake City, Kolkata 700 098, India

[‡]Department of Condensed Matter Physics and Material Sciences, S. N. Bose National Centre for Basic Sciences, Block JD, Sector III, Salt Lake City, Kolkata 700 098, India

[§]Solid State and Structural Chemistry Unit, Indian Institute of Science, Bangalore 560 012, India

Supporting Information

ABSTRACT: Here, we report the synthesis of $TiO_2/BiFeO_3$ nanoheterostructure (NH) arrays by anchoring $BiFeO_3$ (BFO) nanoparticles on TiO_2 nanotube surface and investigate their pseudocapacitive and photoelectrochemical properties considering their applications in green energy fields. The unique TiO_2/BFO NHs have been demonstrated both as energy conversion and storage materials. The capacitive behavior of the NHs has been found to be significantly higher than that of the pristine TiO_2 NTs, which is mainly due to the anchoring of redox active BFO nanoparticles. A specific capacitance of about 440 F g^{-1} has been achieved for this NHs at a current density of 1.1 A g^{-1} with ~80% capacity retention at a current density of 2.5 A g^{-1}. The NHs also exhibit high energy and power performance (energy density of 46.5 Wh kg^{-1} and power density of 1.2 kW kg^{-1} at a current density of 2.5 A g^{-1}) with moderate cycling stability (92% capacity retention after 1200 cycles). Photoelectrochemical investigation reveals that the photocurrent density of the NHs is almost 480% higher than the corresponding dark current and it shows significantly improved photoswitching performance as compared to pure TiO_2 nanotubes, which has been demonstrated based the interfacial type-II band alignment between TiO_2 and BFO.

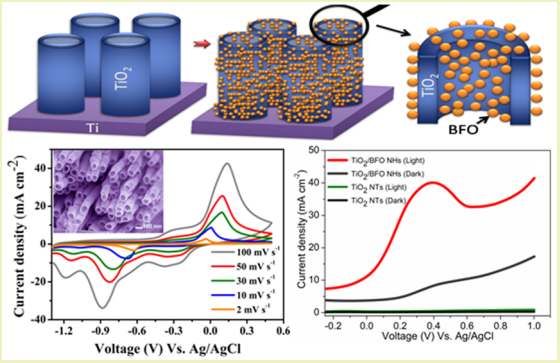

KEYWORDS: *Nanoheterostructures, Multifunctional, Supercapacitor, Photoelectrochemical, Photoelectrode*

INTRODUCTION

Intensive research attention has been focused on the energy storage and conversion from the renewable and clean energy sources in order to deal with the ever-increasing energy consumption and environmental issues.[1,2] Recently, hybrid supercapacitors (SCs) having high energy and high power density, which can bridge the gap between rechargeable battery and ordinary dielectric capacitor, are being considered to be one of the pioneers in the field of alternative energy storage systems in lieu of the conventional rechargeable battery and fuel-cell to quench the energy-thirst of the battery powered electronic gadgets, hybrid vehicles, mechatronic systems and medical instruments.[3,4] Among SCs, the pseudocapacitors have gained remarkable attention because of their high theoretical specific capacitance, high energy and power density and long life cycle associated with Faradaic redox reactions compared to the electrical double-layer capacitors (EDLCs).[5−8] Being inspired by the high pseudocapacitance of various transition metal oxides such as MnO_2, Fe_2O_3, NiO, Co_3O_4, $NiCo_2O_4$ and V_2O_5, researchers have studied them extensively as promising candidates for SC electrodes that are also economical, environment friendly, abundant in nature and can be fabricated using easy, cost-effective routes.[7,9,10] However, the performance of the SCs depends upon many basic characteristics of the electrode. The ideal SCs should have the merits of high specific capacitance, high power density, high energy density, fast ionic conductivity, good rate capability and long cycling stability.[11] To achieve these, various novel nanostructures and nanoheterostructure pseudocapacitor electrodes have been designed based on the transition metal oxides and hydroxides such as, α-Fe_2O_3−MnO_2, carbon NTs−$NiO_x(OH)_y$ etc.[12,13] In this context, the electrodes with 3D nanoheteroarchitectures with large surface area integrated with easy pathway for charge carriers could be ideal for high performance SC electrode.[14−16]

Along with the energy storage, efficient conversion of the green energy has also become very challenging in recent time and considering this the photoelectrochemical (PEC) conversion of the solar energy by using nanostructures of

Received: June 10, 2015
Revised: August 5, 2015
Published: August 14, 2015

DOI: 10.1021/acssuschemeng.5b00519
ACS Sustainable Chem. Eng. 2015, 3, 2254−2263

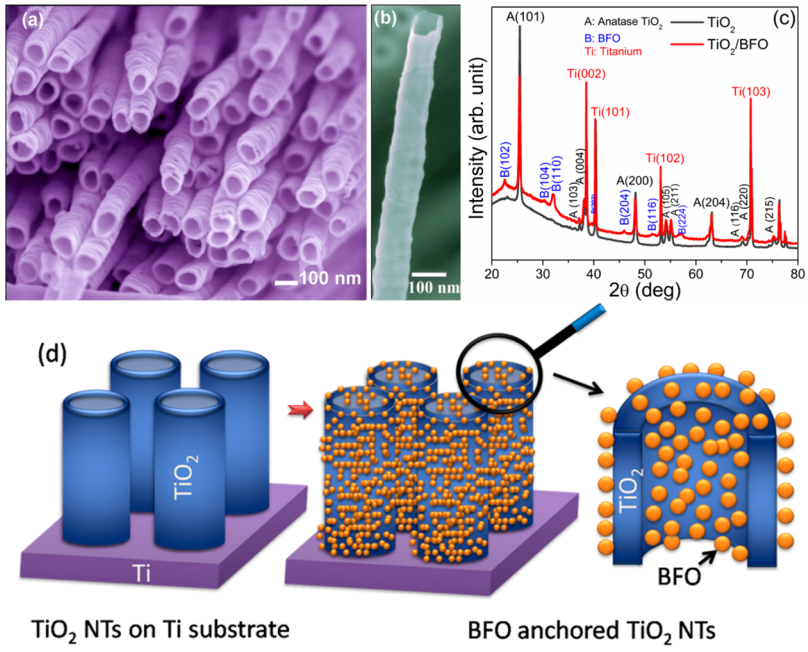

Figure 1. (a and b) FESEM images of the as-prepared 3D arrays of TiO_2/BFO NHs. (c) XRD patterns of the TiO_2 NTs and TiO_2/BFO NHs. (d) Schematic representation of the anchoring of BFO NPs on the surface of TiO_2 NTs.

semiconducting materials as photoelectrodes has also drawn immense attention in the research of photovoltaic devices.[17,18] The performance of photoelectrodes mainly depends upon the suitable choice of the semiconductors having suitable band gaps capable of absorbing a wide range of visible light spectrum that could facilitate effective creation of free charge carriers. In this regard, type-II semiconductor nanoheterojunctions are found to exhibit excellent PEC characteristics because of their preferential band alignment, better photon absorption capability, large interfacial area for rapid charge separation/injection, and improved charge carrier transport.[17−21]

However, among the potential members TiO_2 based nanostructures and NHs have been investigated based on their PEC properties.[17,22] Along with this, few a TiO_2 based NHs like RuO_2−TiO_2 and NiO−TiO_2[23,24] have also been studied as the electrode for SCs, where the redox active elements are responsible for the pseudocapacitance. Very recently, perovskite bismuth ferrite ($BiFeO_3$, BFO) has gained considerable attention as the ferroelectric and photovoltaic material.[25−27] However, still to date, no BFO based electrodes have been reported as a pseudocapacitor or photoelectrode, although BFO containing redox active ions could serve as a SC electrode for energy storage. Moreover, the type-II semiconductor NHs based on BFO and TiO_2 could be interesting considering the PEC properties, arising because of the unique nanoarchitecture, suitable band gap and interfacial band engineering.

In this work, 3D nanoarchitectures of BFO nanoparticles (NPs) anchored TiO_2 nanotubes (NTs) (TiO_2/BFO semiconductor NHs) have been fabricated by facile wet chemical route. The TiO_2/BFO NHs have been demonstrated as an efficient electrode material for the supercapacitor, for the first time, to the best of our knowledge. The 3D nanoarchitecture of TiO_2/BFO NHs provide large surface area for fast charge transfer during Faradaic redox reactions whereas the TiO_2 NTs cores serve as the ideal channel for effective carrier transport to the current collector. The NHs electrode exhibits specific capacitance as high as 440 F g^{-1} at a current density of 1.1 A g^{-1}, excellent rate capability (80% capacity retention at 2.5 A g^{-1}) and moderate cycling stability (~7.5% loss after 1200 cycles) because of the unique 3D nanoarchitecture with enhanced surface area and reduced electron and ion transport pathways. Moreover, the visible light driven PEC property of the TiO_2/BFO NHs has also been investigated here. In this photoelectrode, BFO NPs anchored on the TiO_2 NTs surface provides a 3D nanoarchitecture with large surface area for photon interaction. BFO with a suitable energy band gap effectively absorbs visible light and generates electron−hole pairs, and the type-II n−n band alignment between TiO_2/BFO enables fast carrier separation at the interface through heterojunction engineering.

EXPERIMENTAL SECTION

Reagents. Titanium foil (Alfa Aesar, 99.96% pure and 0.25 mm thick), ammonium fluoride (NH_4F, LobaChemie), formamide (CH_3NO, LobaChemie), bismuth(III) nitrate pentahydrate ($Bi(NO_3)_3{\cdot}5H_2O$, Sigma-Aldrich), iron(III) nitrate nonahydrate ($Fe(NO_3)_3{\cdot}9H_2O$, Merck), 2-methoxyethanol ($C_3H_8O_2$, Merck). The chemicals used throughout the experiment were of analytical grade and no further purification was done.

Synthesis of TiO_2 NTs. The TiO_2 NTs arrays were fabricated by electrochemical anodization of high purity Ti foil. A piece of Ti foil of dimensions 40 × 60 × 0.25 mm, pretreated with several cleaning processes, was used as the anode in a formamide based electrolyte bath containing 0.2 M of NH_4F and 5 vol % of DI water. A high purity copper foil of similar dimension acted as the cathode. Anodization was carried out under a constant voltage of 25 V at 20 °C for 20 h. After the as-anodized sample was cleaned in ethanol and acetone, it was annealed in air in a tube furnace at 400 °C for 90 min.

Synthesis of TiO_2/BFO NHs. The TiO_2/BFO NHs arrays were fabricated by a facile wet chemical route. In this process, the as-prepared arrays of TiO_2 NTs were dipped in a 0.3 M solution of bismuth(III) nitrate pentahydrate with 0.3 M iron(III) nitrate nonahydrate in 2-methoxyethanol at room temperature for 4 h. Afterward, the dip-coated sample was dried under IR lamp and annealed for 2 h in a tube furnace at 480 °C in air.

DOI: 10.1021/acssuschemeng.5b00519
ACS Sustainable Chem. Eng. 2015, 3, 2254−2263

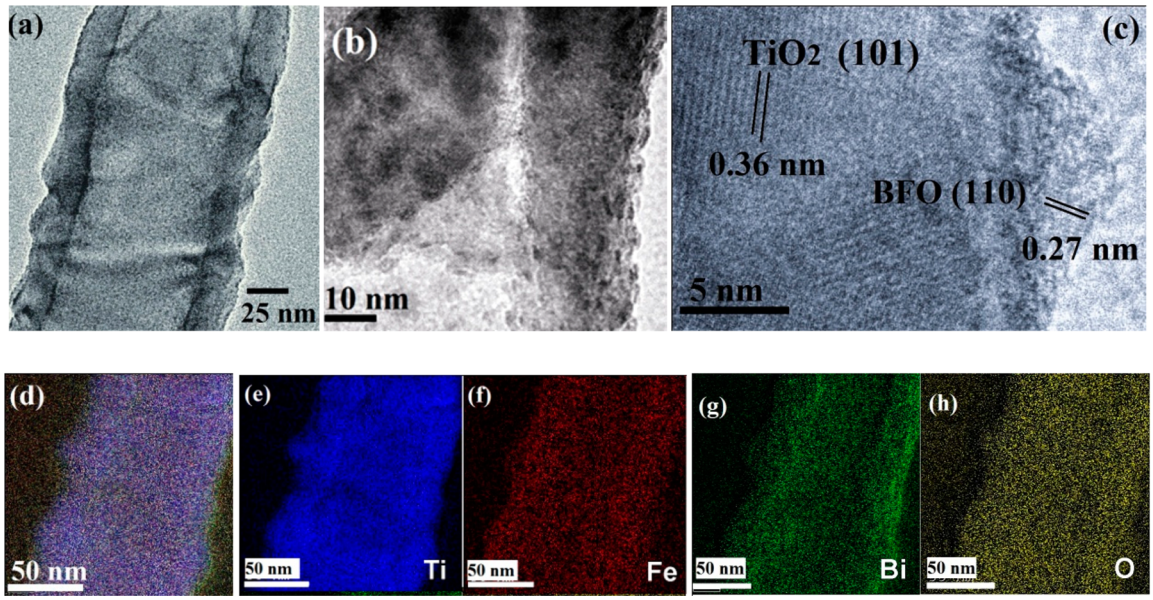

Figure 2. (a, b and c) TEM micrographs of the as prepared TiO_2/BFO NHs. (d, e, f, g and h) EFTEM micrographs of the TiO_2/BFO nanoheterostructures.

Material Characterizations. The morphology, structure and crystal structure of the TiO_2/BFO NHs array were studied by field emission scanning electron microscopy (FESEM, JEOL JSM-7600F) and high resolution transmission electron microscopy (HRTEM, JEOL JEM 2100). The selected area electron diffraction (SAED) pattern and the energy filtered transmission electron microscopy (EFTEM) images for the sample were also obtained using the HRTEM. The chemical composition of the sample was studied by energy dispersive X-ray spectroscopy (EDS, Oxford Instruments, attached to the FESEM) and X-ray photoelectron spectroscopy (XPS) using the monochromatic X-ray from VG-SCIENTA, USA (SCIENTA MX-650) with Al Kα X-ray beam (1486.6 eV). The beam current used was 20 mA. Raman spectroscopy measurements were carried out in the range of 50−1000 cm^{-1} using a micro-Raman spectrometer (LABRAM HR from Horiba Jobin Yvon). The crystal phases present in the sample were investigated by X-ray diffraction (XRD, Panalytical X'Pert Pro diffractometer) using Cu Kα line (λ = 1.54 Å). The absorbance spectrum of the TiO_2/BFO NHs was recorded at room temperature by a UV−visible-NIR spectrometer (PerkinElmer Lambda 1050 UV/vis/NIR spectrometer) within a wavelength limit of 800 to 250 nm.

Electrochemical and Photoelectrochemical Measurements. The electrochemical and photoelectrochemical properties of TiO_2/BFO NHs were analyzed through potentiostatic and galvanostatic measurements using a software controlled conventional three electrode electrochemical cell (Potentiostat, Metrohm AutoLab-30) consisting of the as-prepared sample as the anode, Ag/AgCl as the reference electrode and a Pt wire as the cathode and an aqueous solution of 0.5 M Na_2SO_4 as the electrolyte at room temperature. The linear sweep voltammetry (LSV) was executed with the same workstation under dark and visible white light illumination (λ > 420 nm with fixed intensity of 10 mW/cm^2) conditions. The photo-switching property was also investigated at zero bias voltage vs Ag/AgCl with 100 s interval between light "on−off" cycles. Electrochemical impedance spectroscopy (EIS) of the TiO_2/BFO NHs was carried out to investigate the charge carrier generation and transfer procedures under visible light and dark conditions within a frequency range of 10 mHz to 100 kHz with an ac amplitude of 0.5 V. The mass of the active materials were calculated by subtracting the mass of the underneath Ti foil from the total mass of the electrode (i.e., TiO_2 on Ti or TiO_2/BFO on Ti) by using a microbalance. The mass of the Ti foil was calculated after peeling off the active materials from its surface. The loading density of TiO_2 on Ti is 3.2 mg/cm^2 and same for TiO_2/BFO on Ti is 3.3 mg/cm^2.

RESULTS AND DISCUSSION

The morphology of the as-prepared TiO_2/BFO 3D NHs studied by using field emission scanning electron microscopy (FESEM), as shown in Figure 1a,b, reveal regular vertical tubular arrays of the NHs with uniform shape and diameter grown over a large surface area (see Figure S1, Supporting Information for the top view images). The surface roughness of the single NH (Figure 1b) indicates the anchoring of the BFO NPs on the surface of TiO_2 NTs grown vertically on the Ti substrate, as shown schematically in Figure 1d. The outer diameters of the NHs are found to be ∼110 nm with a wall thickness of about 20−25 nm. The XRD patterns for both the TiO_2 NTs and TiO_2/BFO NHs have been shown in Figure 1c. Presence of polycrystalline anatase phase of TiO_2 is evidenced from the XRD pattern where the BFO nanoparticles are also found polycrystalline in nature with peaks correspond to the distorted rhombohedral structure of $BiFeO_3$ with *R*3*c* space group (JCPDS No: 71-2494). The peaks for Ti arise because of the Ti substrate underneath the NHs. However, the formation of TiO_2/BFO heterojunction can better be visualized from the transmission electron microscopy (TEM) micrographs (Figure 2a,b,c and Figure S2a in the Supporting Information). Clear indication of the anchoring of BFO NPs throughout the surface of the TiO_2 NTs in a regular way is evidenced from Figure 2b,c. The size of the BFO NPs is found to be ∼2−8 nm from the high resolution TEM micrograph (Figure 2b,c and Figure S2a in the Supporting Information). The SAED patterns for the TiO_2/BFO 3D NHs and TiO_2 NTs are shown in Figure S2b in the Supporting Information. The uniform anchoring of the BFO NPs on TiO_2 NTs surface has further been visualized by the energy filtered TEM (EFTEM) studies (Figure 2d−h) where it can be seen that all the component elements of the NHs viz. Ti, Fe, Bi and O are present in a regular way throughout the NHs. Furthermore, the presence of the component elements has also been evidenced from the energy

DOI: 10.1021/acssuschemeng.5b00519
ACS Sustainable Chem. Eng. 2015, 3, 2254−2263

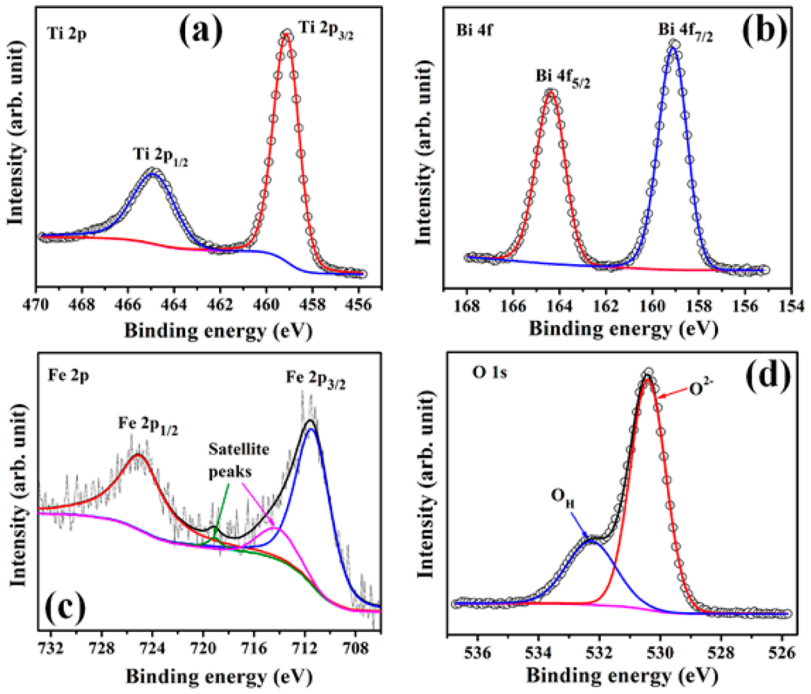

Figure 3. XPS spectra of (a) Ti 2p, (b) Bi 4f, (c) Fe 2p and (d) O 1s core levels of the TiO_2/BFO NHs.

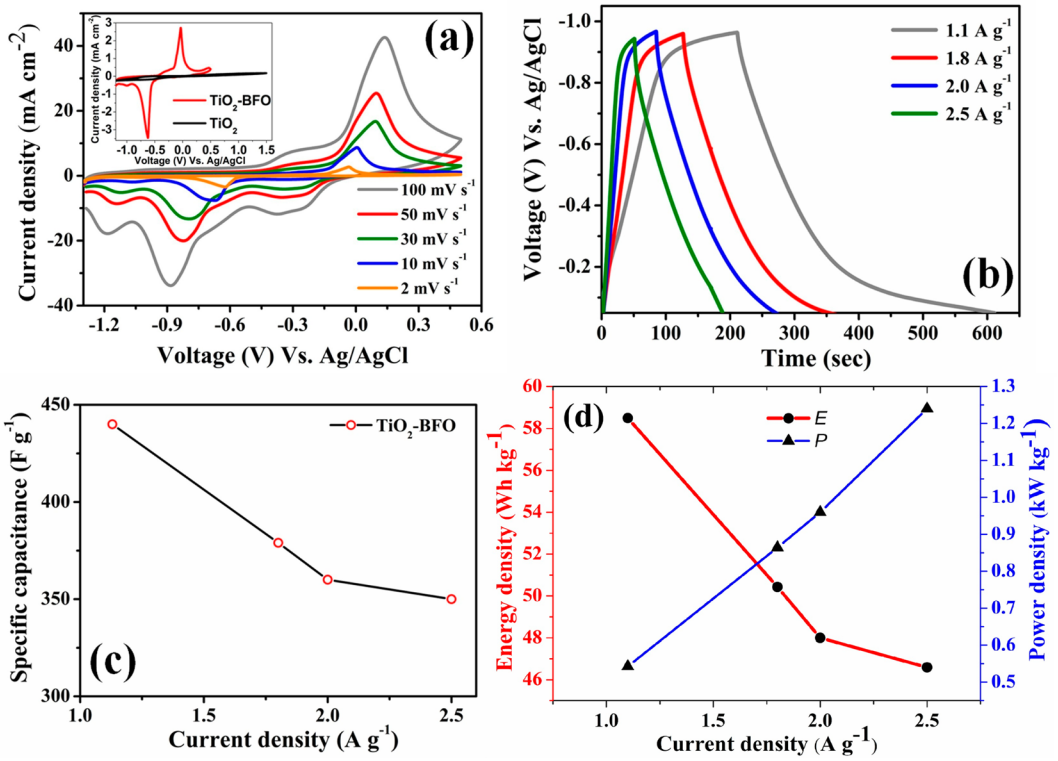

Figure 4. (a) Cyclic voltammetry curves of the as-prepared TiO_2/BFO NHs electrode at different scan rates in a 0.5 M Na_2SO_4 solution at room temperature, (inset of panel a) comparison between the CV curves of TiO_2 and TiO_2/BFO NHs electrode at scan rate of 2 mV s^{-1}. (b) Constant current charge/discharge curves of the as-prepared TiO_2/BFO NHs electrode at different current densities. (c) Variation of specific capacitance with charge/discharge current densities. (d) Variation of energy and power densities with charge/discharge current densities for TiO_2/BFO NHs electrode.

dispersive X-ray spectroscopy (EDS) analysis (Figure S3, Supporting Information).

Raman spectroscopy has been employed to understand the lattice properties and spin-phonon coupling of the pure TiO_2 NTs and TiO_2/BFO NHs. The intense six active Raman modes (Figure S4, Supporting Information) of TiO_2 NTs namely $E_g(1) \sim 144$ cm^{-1}, $E_g(2) \sim 196$ cm^{-1}, $B_{1g}(1) \sim 397$ cm^{-1}, $A_{1g}(2)$ and $B_{1g}(2) \sim 518$ cm^{-1} and $E_g(3) \sim 636$ cm^{-1} are

DOI: 10.1021/acssuschemeng.5b00519
ACS Sustainable Chem. Eng. 2015, 3, 2254−2263

assigned to anatase TiO_2. The increase of the intensity, shift in position and the broadness of the $E_g(1)$ phonon mode of TiO_2 after the anchoring of BFO NPs is most expectedly because of the contribution from the longitudinal-optical (A_1) phonon modes such as A_1-1 (125 cm^{-1}) and A_1-2 (158 cm^{-1}) of BFO (inset of Figure S4, Supporting Information).[28,29]

For a better insight of the chemical composition and electronic structure of the as-synthesized TiO_2/BFO NHs, we have performed the X-ray photoelectron spectroscopy (XPS) analysis. The XPS survey spectrum (Figure S5, Supporting Information) clearly shows the presence of all the constituent elements like Ti, Bi, Fe and O. The high resolution curve-fitted elementary XPS peaks of Ti 2p, Bi 4f, Fe 2p and O 1s core levels are presented in Figure 3. In Figure 3a, the binding energies of the Ti $2p_{3/2}$ and Ti $2p_{1/2}$ are found to be nearly 459 and 464.8 eV, respectively, which correspond to the +4 oxidation state of Ti in anatase TiO_2.[30−32] However, there is no sign of the presence of Ti^{3+} state which usually occurs at 457.4 eV[31] Figure 3b shows the 4f core level spectrum of bismuth where the peaks corresponding to the Bi $4f_{7/2}$ and Bi $4f_{5/2}$ situated at the binding energies of 159 and 164.3 eV, respectively, clearly represent the +3 oxidation state of Bi in $BiFeO_3$ without any trace of metallic Bi in the matrix.[28,33] The deconvolution of the Fe 2p core level spectrum produces four Gaussian peaks, as shown in Figure 3c. The positions of the characteristics peaks of Fe $2p_{3/2}$ and Fe $2p_{1/2}$ have been found in the vicinity of 711.1 and 725 eV, respectively, correspond to the trivalent oxidation state of iron in $BiFeO_3$.[34,35] Besides these, two tiny satellite peaks can also be observed at the binding energies of 714.2 and 719 eV, redefining the electronic structure of Fe^{3+}. Moreover, there is no sign of the Fe^{2+} related peaks (at 709.5 eV for Fe $2p_{3/2}$ and 716 eV for Fe $2p_{1/2}$), which again confirms the presence of only trivalent oxidation state of iron in BFO.[34,35] The XPS analysis indicates that only pure $BiFeO_3$ phase is present without any type of impurities. The XPS spectrum of O 1s core level, as shown in Figure 3d, can be deconvoluted into two symmetric Gaussian peaks centered on 530.3 and 532.2 eV. The low binding energy peak at 530.3 eV of O 1s can be assigned to the −2 oxidation state of oxygen in the NHs.[31,36] The peak around 532 eV can be ascribed to the presence of the hydroxyl group due to absorbed moisture or the oxygen vacancy related defects in NHs.[31,32,28]

The electrochemical properties of the TiO_2/BFO 3D NHs elctrode have been studied by using the cyclic voltammetry (CV) and galvanostatic (GV) charge/discharge methods to investigate the performance of NHs as a SC. Figure 4a shows the CV curves of the TiO_2/BFO NHs electrode, recorded at different scan rates of 2, 10, 30, 50 and 100 mV s^{-1} within a voltage window of −1.3 to +0.5 V in 0.5 M aqueous Na_2SO_4 solution at room temperature and the corresponding CV curves for pristine TiO_2 NTs are also given in Figure S6 (Supporting Information). In Figure 4a, the typical shape of these CV curves consisting of distinct redox peaks represents pseudocapacitive behavior of this NHs. Here, pseudocapacitance mainly arises because of the surface and near surface based Faradaic oxidation/reduction reactions between variant oxidation states of the Bi and Fe together with the proton movement between the electrodes through electrolyte.[37] At the same time, electrons move from the electrode to the current collector (Ti substrate) and vice versa to balance the chemical equilibrium. Though in case of BFO the actual redox reaction mechanism is not known yet, however, a proposed charge storage mechanism of BFO might involve the redox reaction between III and 0 and III and II oxidation states of Bi and Fe, respectively.[12,38−40]

It is evident from Figure 4a that the current response of the electrode increases with increasing scan rates and the shapes of cyclic voltammogram curves remain almost invariant throughout the whole range of scan rates (2 to 100 mV s^{-1}). A lower current at a lower scan rate is mainly because of the thick diffusion layer grown on the electrode surface, which limits electrolyte flux toward the electrode. However, at higher scan rates, the diffusion layer cannot grow wider on the electrode surface, facilitating higher electrolyte flux and hence the enhancement in current. Significant increase in current density has been observed in the case of the TiO_2/BFO NHs electrode as compared to the pristine TiO_2 nanotube based electrode (corresponding CV scans at 2 mV s^{-1} are shown in the inset of Figure 4a) after anchoring BFO on their surface. Introduction of BFO NPs over the TiO_2 NTs surface significantly increases the active area of the reaction platform for the surface or near surface based redox reactions and thus the capacitive performance is found to enhance.[12,16] Moreover, the unique 3D structure of the electrode materials can store the electrolytic ions effectively and also facilitates ion transfer to the inner sides of the electrode by shortening ion diffusion path even at higher scan rates. However, in Figure 4a it is found that with the increase in scan rate the upper and lower redox peaks shift more toward positive and negative sides, respectively, which is mainly because of the development of overpotential that limits the faradaic reactions. Actually, at higher scan rates, different types of polarization effects (concentration polarization, charge transfer polarization etc.) dominate, which increases the overpotential impeding the Faradaic reactions to happen leading to the increase in peak separation. However, we have observed nearly linear dependence of the anodaic and cathodaic peak currenton the potential scan rates, as shown in Figure S7 (Supporting Information), which confirms surface controlled pseudocapacitive behavior of the material under investigation.[6,41]

Figure 4b shows the typical galvanostatic charge/discharge cycling curves of the as-prepared TiO_2/BFO electrode at different current densities ranging from 1.1 to 2.5 A g^{-1} within the voltage window of 0 to −1 V. The potential-time plots of TiO_2/BFO NHs electrode exhibitasymmetric behavior between charge/discharge profiles, characterized by slow discharging process with an extended tail as compared to the charging. This slow rate of discharging exhibits higher Coulombic efficiency (>100%) for the electrode, which can be explained based on the change in the oxidation states of the constituent redox active elements during cathodic and anodic scans of the cyclic voltammograms of NHs electrode (Figure 4a). During charging, mainly all the Bi metals lost electrons and completely converted into Bi^{3+} ions as represented by a distinct single peak in the anodic sweep in CV curves, whereas during discharging, though the majority of Bi^{3+} ions reduced to Bi metal by gaining electrons (large peak at ∼ −0.87 V during cathodic sweep in CV curves), some Bi^{3+} ions still remained unaltered and were converted to Bi metal at some higher negetive voltages (small peak at ∼ −1.2 V during cathodic sweep in CV curves). This type of two step reduction procedure helps to hold the charge for longer times leading to the extended tail of discharging curves.[16,39,40,42] Now, from the discharging curves, the specific capacitance (C_{sp}) was calculated using eq 1.

DOI: 10.1021/acssuschemeng.5b00519
ACS Sustainable Chem. Eng. 2015, 3, 2254−2263

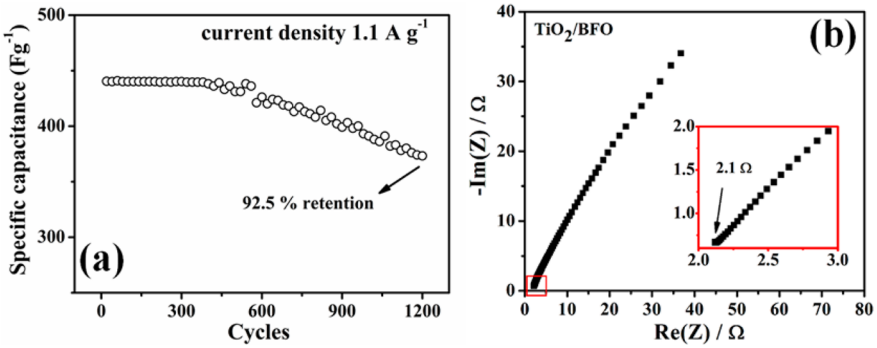

Figure 5. (a) Cycling performance of TiO_2/BFO NHs electrode showing the capacitance retention after 1200 cycles using a charge/discharge at current densities of 1.1 A g^{-1}. (b) Electrochemical impedance spectroscopy (Nyquist plot) for the supercapacitor electrode based on TiO_2/BFO NHs electrode under normal conditions (dark condition).

$$C_{sp} = \frac{I\Delta t}{m\Delta V} \quad (1)$$

where I (A) is the discharge current, Δt (s) is the discharge time consumed in the potential window of ΔV (V) and m (g) is the mass of the active material. The calculated specific capacitance (C_{sp}) of as prepared TiO_2/BFO NHs electrode as a function of current density is shown in Figure 4c. In this case, maximum value of specific capacitance was found to be nearly 440 F g^{-1} at a current density of 1.1 A g^{-1} and this remains at 350 F g^{-1} when the current density was increased to 2.5 A g^{-1}, implying that this NHs electrode can retain ∼80% of its initial capacitance when the current density is almost 2.3 times higher than the initial value. The specific capacitance of the TiO_2/BFO NHs electrode is found to be much better than the values as reported for other BFO based supercapacitors, such as BFO thin films[37] and also for other pervoskite based electrodes.[43−46] Moreover, The specific capacitance of the TiO_2/BFO NHs electrode is found to be higher than the carbon based electrodes like carbon nanotube-bridged graphene 3D material (∼199 F g^{-1})[47] and graphene/carbon nanotube electrode (∼115 F g^{-1})[48] but lower than the cobalt oxide based electrode (∼768 F g^{-1}).[49] The excellent capacitive performance (high specific capacitance and high capacitive retention) of the TiO_2/BFO NHs electrode can mainly be attributed to the nanoarchitectural design of the electrode where the BFO anchored TiO_2 NTs surface provides a large and fast redox reaction environment together with the Ti metal underneath, which serves as the highly conductive current collector. Moreover, direct growth of the TiO_2 NTs on the Ti current collector significantly reduces the series resistance of the whole electrode, as represented by the small IR drop in the charging/discharging curves, also enhances the capacitive performance by allowing fast charge transfer. However, for practical applications, it is important for a supercapacitor to possess high energy delivery capability in addition to high specific capacitance at high current density. Therefore, calculation of energy and power densities of the supercapacitor electrode gives the idea about the feasibility of applying this NHs electrode for practical device fabrication. Here, we have calculated the energy and power densities of this NHs electrode from the galvanostatic charge/discharge curves using eqs 2 and 3 as follows

$$E = \frac{1}{2}C_{sp}(\Delta V)^2 \quad (2)$$

and

$$P = \frac{E}{\Delta t} \quad (3)$$

where E (Wh kg^{-1}), P (kW kg^{-1}), C_{sp} (F g^{-1}), ΔV (V) and Δt (s) are the energy density, power density, specific capacitance, the potential window of discharge and time of discharge, respectively. Figure 4d shows that the energy density of the TiO_2/BFO NHs electrode decreases from 58.5 to 46.5 Wh kg^{-1} as the discharge current density increases from 1.1 to 2.5 A g^{-1}, whereas the power density goes up to 1.2 kW kg^{-1} at a current density of 2.5 A g^{-1}. Indeed, the calculated energy and power densities of this electrode are found to be far better than the previously reported perovskite based supercapacitors.[37,43−46] This type of high energy and power performance at higher current density of this NHs electrode indicates the potential of this electrode for application in electrochemical supercapacitors.

Long cycle life is one of the vital characteristics that an ideal supercapacitor should have. Figure 5a shows the life cycle test of the as prepared TiO_2/BFO NHs electrode, carried out for 1200 cycles at a current density of 1.1 A g^{-1}. Almost 92% capacitance retention has been observed for this TiO_2/BFO NHs electrode after 1200 cycles. This decay of capacitance after 1200 cycles can be attributed to the dissolution/decomposition of some electroactive material into the electrolyte during continuous charge/discharge test. Hence, considering the long cycle stability, the TiO_2/BFO NHs electrode can be considered as a moderate type pseudocapacitive material in aqueous electrolyte medium.

The electrical conductivity and ion transfer of the supercapacitor electrodes has been investigated further by electrochemical impedance spectroscopy (EIS). All the impedance measurements were carried out at open circuit potential within a frequency range of 10−10^5 Hz with an voltage amplitude of 5 mV and the corresponding Nyquist plot for the TiO_2/BFO NHs electrode is shown in Figure 5b. The intercept of the impedance curve on the real axis in the high frequency range represents the equivalent series resistance (ESR) of the system, which includes the bulk resistance of the electrolyte, the inherent resistances of the electrode active material along with the contact resistance at the interface between electrolyte and electrode.[50] Under normal conditions, the magnitude of the ESR for TiO_2/BFO NHs electrode is found to be 2.1 Ω, which represents good electrical contacts and higher electrical conductivity. Such low resiatance of the NHs system significantly improves the ion diffusion and electron conduction procedure which has been reflected by the higher power density

DOI: 10.1021/acssuschemeng.5b00519
ACS Sustainable Chem. Eng. 2015, 3, 2254−2263

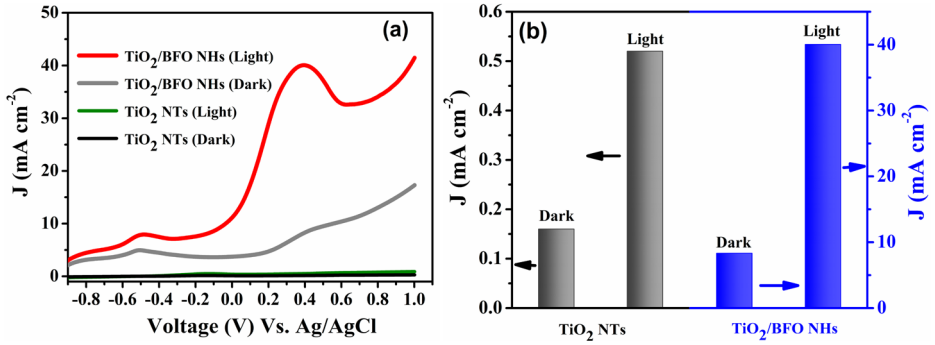

Figure 6. (a) Current density (J) vs bias voltage (V) plot for the TiO_2 NTs and TiO_2/BFO NHs array under dark and visible white light (λ > 420 nm) illumination conditions and (b) comparison between dark and photocurrent densities of the electrodes in 0.5 M Na_2SO_4 solution at a bias potential of 0.4 V (vs Ag/AgCl).

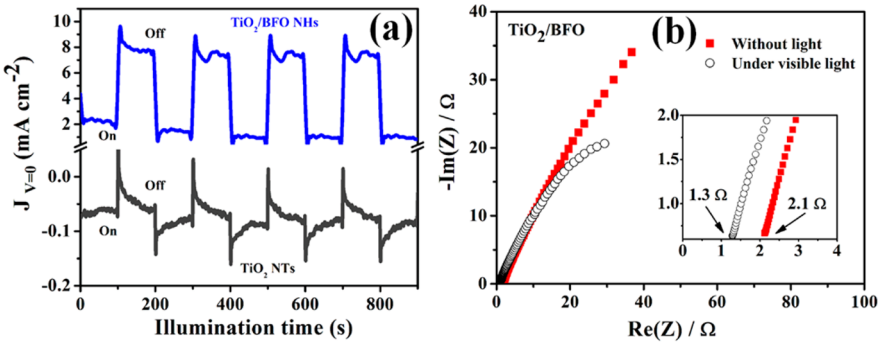

Figure 7. (a) Zero-bias photocurrent density as a function of illumination time for the TiO_2 NTs and TiO_2/BFO NHs arrays; (b) Nyquist plots under visible light and without light (dark) conditions for the TiO_2/BFO NHs arrays. Inset shows the magnified view of the high frequency region of the impedance spectrum.

of the NHs electrode. However, the arc in the low frequency regime of the Nynquist plot of TiO_2/BFO NHs electrode clearly indicates the charge transfer resistance of the electrode material resulting from the diffusion of electrons.

The photoelectrochemical energy conversion and the photoswitching performance of the pristine TiO_2 NT and TiO_2/BFO NHs arrays were investigated by employing the same workstation mentioned earlier. To investigate the photoelectrochemical activities of pristine TiO_2 NT and TiO_2/BFO NHs, linear sweep voltammetry (LSV) analyses were performed under dark and white visible light (λ > 420 nm with fixed intensity of 10 mW/cm^2) illumination conditions at room temperature and the corresponding current density vs voltage (J–V) curves are shown in Figure 6a recorded at a constant potential of 0.3 V vs Ag/AgCl. Here, one thing should be noted: that the sudden boost in current at around 0.4 V for TiO_2/BFO NHs can be attributed to the surface based Faradaic reactions that has also been observed during CV measurements (as discussed earlier). The variation in current density of both the electrodes under dark and visible light illumination conditions at a particular bias voltage is shown in Figure 6b. From Figure 6a,b, it is evident that the current densities of pure TiO_2 NT arrays under dark and even in illuminated conditions are literally nominal compared to the TiO_2/BFO NHs. For TiO_2 NT arrays, change in current density is also very small after illumination. But, for TiO_2/BFO NHs, the photocurrent density at 0.4 V is found to be about 480% higher than the corresponding dark current. Therefore, considering the whole range of external bias voltage (−0.9 to +1 V) we can conclude that the conversion capability of visible light through photogenerated charge carrier generation and separation of TiO_2/BFO NHs is significantly higher than the TiO_2 NTs, which is mainly because of the introduction of the suitable band gap BFO NPs over the TiO_2 NTs surface. The photocurrent density recorded for the TiO_2/BFO NHs electrode is found to be considerably higher than that of the $SrTiO_3$/TiO_2 nanotube arrays[51] and surface modified TiO_2 NWs.[52] The photocurrent density is found to be comparable with that of the ZnO/CdTe electrode.[53] The photoconversion efficiency, η of the TiO_2/BFO NHs electrode is calculated by using the following formula:

$$\eta = (I_{ph} \times V)/P_{in} \quad (4)$$

where I_{ph} is the photocurrent density, V is the voltage difference between anode and cathode and P_{in} is the input power density (10 mW/cm^2). Hence, the value of η is calculated as 8.7%, at a voltage difference of 0.1 V vs Ag/AgCl electrode where the value of photocurrent density is found to be 8.7 mA/cm^2.

As far as the photoswitching is concerned, the TiO_2/BFO NHs array is found to be superior to the pristine TiO_2 NTs. The photoanodes exhibit a symmetric photoswitching characteristic on application of a periodic light "on–off" cycle. Figure 7a shows the current density vs time (J–t) plots for pristine TiO_2 NTs and TiO_2/BFO NHs arrays at 0 V vs Ag/AgCl. One reason behind choosing zero bias is that it means the external visible solar energy can be harvested without applying any bias to the electrochemical cell. It is evident from Figure 7a that for TiO_2/BFO NHs, there exist sharp changes in current density when the visible light is switched "on" and "off", representing fast photoswitching characteristics of the TiO_2/BFO NHs. The increments in current density after switching "on" the light

DOI: 10.1021/acssuschemeng.5b00519
ACS Sustainable Chem. Eng. 2015, 3, 2254–2263

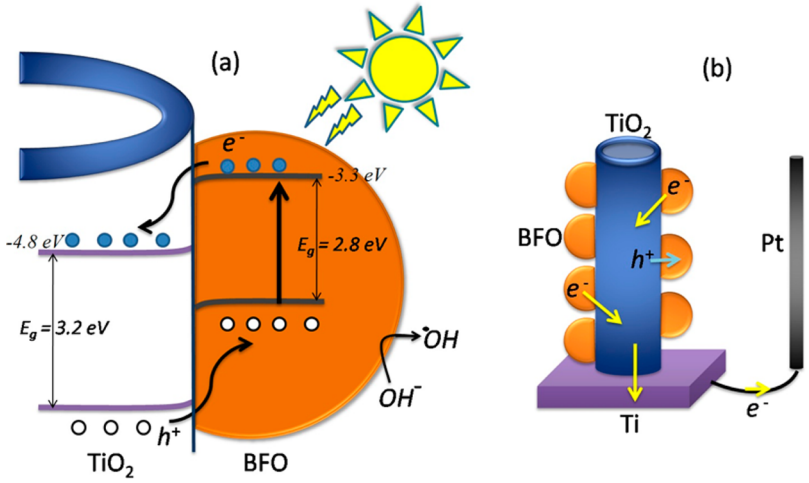

Figure 8. (a) Schematic diagram of the type-II band configuration between TiO_2 and BFO and the electron−hole migration across the interface under visible light illumination. (b) Circuit diagram consisting of TiO_2/BFO NHs and other components.

source are always found to be at least greater than 500% as compared to "off" state. After the visible light is switched "on", the current initially rises to a transient maximum and then it tends to saturate during each interval of "on" cycle. However, the decrements in the current density from the transient maximum to the saturated state, just before switch "off", has been found to be almost 17% with a time constant associated with the transient component is ∼10 s. In the case of the pristine TiO_2 NTs array, a poor photoswitching characteristic is observed, as shown in Figure 7a. In this case, the photocurrent density is almost 8−10 times smaller than that for the TiO_2/BFO NH array, but the increments in current density to the transient maximum after switching "on" the visible light are around 100% only. More significantly, as time goes on, the current density for TiO_2 NT arrays does not show any sign of saturation and keeps dropping off severely during the light "on" state and this drop is almost 300% between just after the "on" and just before "off" states with a time constant of ∼75 s. This undoubtedly implies a poor current retention property and as a result a poor photoswitching performance of pristine TiO_2 NTs.

For further elucidation on the photoelectrochemical properties of TiO_2/BFO NHs governed by enhanced charge carrier dynamics after illumination, we performed the EIS analysis of the NHs under dark and illuminated conditions and the corresponding Nyquist plots are shown in Figure 7b. It is evident that under visible light the arc radius of Nyquist plots of the electrode is significantly smaller than that for the dark condition, representing lower charge-transfer resistance of the TiO_2/BFO NHs electrode during illumination, which is ideal for fast charge carrier transport. On the other hand, the large diameter semicircle under dark condition reflects larger charge-transfer resistance resulting in poor charge transportation capability and poor current response. More interestingly, from the inset of Figure 7b, it can be seen that the ESR of the NHs decreases from 2.1 to 1.3 Ω after visible light illumination, which is mainly due to the incorporation of BFO NPs having energy band gap suitable for absorbing visible light and the improved charge carrier dynamics because of the interfacial band engineering as discussed below.

The enhanced photocurrent in TiO_2/BFO NHs can be attributed to various factors such as (a) the type-II *n*−*n* band alignment between TiO_2 NTs and BFO nanostructures, which efficiently facilitates the photogenerated charge carrier (electron−hole) separation and transfer phenomena, (b) a suitable band gap of BFO as compared to TiO_2 for better absorption of incident solar energy and (c) the presence of BFO nanoparticles outside of the TiO_2 NTs, which actually reduces the energy loss by its antireflection property. In details, bulk BFO has an optical band gap (E_g) of 2.7 eV and electron affinity (χ) of 3.3 eV[54] whereas anatase TiO_2 has a band gap of 3.2 eV and affinity of 4.8 eV. Hence, after the heterojunction is formed between TiO_2 and BFO, Fermi levels of both materials have to be the same at thermal equilibrium, which drives band bending toward the TiO_2 side and finally produces a staggered type-II band configuration, as depicted in Figure 8a. The conduction band (CB) minima of BFO lie above that of TiO_2 and the valence band (VB) maxima of BFO also lie above that of TiO_2. With this band configuration, when the TiO_2/BFO NHs is illuminated with visible light (λ > 420 nm), the light gets absorbed by BFO (due to its suitable band gap ∼443 nm) and also by the oxygen vacancy and defect states present in TiO_2 resulting generation of electron−hole (e-h) pairs. In this experiment, the band gap of BFO is found to be ∼2.8 eV from the UV−vis spectroscopy studies (see Figure S8, Supporting Information). The blue shift of the band gap emission in BFO NPs is most expectedly because of the reduced size of the NPs.[28] However, the band-to-band transition in BFO produces more e-h pairs than in TiO_2. Now, as shown in Figure 8a, these photogenerated electrons in the CB of BFO diffuse through the interface to the CB of TiO_2. On the other hand, the holes present in the VB of BFO, react with the OH^- ions present in the electrolyte and reduce them into OH radicals. Thus, BFO again gets ready for absorption of visible light to produce e-h pairs. However, as the holes in the VB of BFO disappear in making OH radicals, a concentration gradient of holes occurs, which helps the holes present in TiO_2 to diffuse into BFO. This phenomenon reduces the recombination probability of the electrons diffused to the TiO_2 from the BFO side. These photogenerated electrons then drift axially downward through to the TiO_2 NT and move to Pt counter electrode via the underneath Ti substrate for hydrogen production ($4e^- + 4H^+ \rightarrow 2H_2$, see Figure 8b).

DOI: 10.1021/acssuschemeng.5b00519
ACS Sustainable Chem. Eng. 2015, 3, 2254−2263

CONCLUSION

Highly ordered 3D arrays of bismuth ferrite nanoparticle anchored TiO_2 NTs have been fabricated by a facile wet chemical route. The electrochemical energy storage and photoelectrochemical energy conversion properties of the TiO_2/BFO nanoheterostructure arrays have been demonstrated successfully. Introduction of redox active BFO nanoparticles having lower energy band gaps as compared to TiO_2 enhances both the pseudocapacitive and photoelectrochemical performance of the nanoheterostructures significantly as compared to the pristine TiO_2 NTs. In this unique nanoarchitecture, BFO nanoparticles having diameters in the range ∼2−8 nm significantly enhance the specific surface area for the surface based Faradaic reactions whereas the TiO_2 NTs cores act both as a mask and the pathways for the electron transportation toward the current collector, making the device suitable for pseudocapacitor electrode. The substantial enhancement in the current density after visible light irradiation on TiO_2/BFO nanoheterostructures is addressed based on several properties of the nanoheterostructures like the suitable band gap of BFO to absorb visible light efficiently and also the type-II heterojunction formation due to the interface engineering, which helps the generation/separation of free charge carriers (electron−hole pairs) allowing unidirectional current flow. This study indicates that the arrays of TiO_2/BFO nanoheterostructure with enhanced capacitive and photoelectrochemical performance holds potential for applications in both renewable energy generation and storage devices.

ASSOCIATED CONTENT

Supporting Information

The Supporting Information is available free of charge on the ACS Publications website at DOI: 10.1021/acssuschemeng.5b00519.

FESEM images of large scale growth of TiO_2/BFO NHs arrays on Ti substrate, TEM and SAED analysis, EDS analysis, Raman spectra, XPS spectrum, cyclic voltammetry curves and corresponding variation of specific capacitance with scan rates, current density vs. scan rate plots, and UV−visible spectra (PDF).

AUTHOR INFORMATION

Corresponding Author

*G. G. Khan. E-mail: gobinda.gk@gmail.com.

Author Contributions

⊥These authors contributed equally to this work.

Funding

Department of Science and Technology (DST), Government of India.

Notes

The authors declare no competing financial interest.

ACKNOWLEDGMENTS

Gobinda Gopal Khan is thankful to the Department of Science and Technology (DST), Government of India, for providing research support through the "INSPIRE Faculty Award" (IFA12-ENG-09). The authors are also thankful to Prof. K. S. R. Menon and Mr. A. K. Kundu of Surface Physics and Materials Science Division, Saha Institute of Nuclear Physics, Kolkata, India for the XPS measurements.

REFERENCES

(1) Jiang, J.; Li, Y. Y.; Liu, J. P.; Huang, X. T.; Yuan, C. Z.; Lou, X. W. Recent Advances in Metal Oxide-based Electrode Architecture Design for Electrochemical Energy Storage. *Adv. Mater.* **2012**, *24*, 5166−5180.

(2) Dunn, B.; Kamath, H.; Tarascon, J. M. Electrical energy storage for the grid: A battery of choices. *Science* **2011**, *334*, 928−935.

(3) Miller, J. R.; Simon, P. Electrochemical Capacitors for Energy Management. *Science* **2008**, *321*, 651−652.

(4) Yu, G.; Hu, L.; Vosgueritchian, M.; Wang, H.; Xie, X.; McDonough, J. R.; Cui, X.; Cui, Y.; Bao, Z. Solution-Processed Graphene/MnO_2 Nanostructured Textiles for High-Performance Electrochemical Capacitors. *Nano Lett.* **2011**, *11*, 2905−2911.

(5) Lang, X. Y.; Hirata, A.; Fujita, T.; Chen, M. W. Nanoporous metal/oxide hybrid electrodes for electrochemical supercapacitors. *Nat. Nanotechnol.* **2011**, *6*, 232−236.

(6) Augustyn, V.; Simon, P.; Dunn, B. Pseudocapacitive Oxide Materials for High-Rate Electrochemical Energy Storage. *Energy Environ. Sci.* **2014**, *7*, 1597−1614.

(7) Yang, L.; Cheng, S.; Ding, Y.; Zhu, X.; Wang, Z. L.; Liu, M. Hierarchical Network Architectures of Carbon Fiber Paper Supported Cobalt Oxide Nanonet for High-Capacity Pseudocapacitors. *Nano Lett.* **2012**, *12*, 321−325.

(8) Zhang, X.; Shi, W.; Zhu, J.; Kharistal, D. J.; Zhao, W.; Lalia, B. S.; Hng, H. H.; Yan, Q. High-Power and High-Energy-Density Flexible Pseudocapacitor Electrodes Made from Porous CuO Nanobelts and Single-Walled Carbon Nanotubes. *ACS Nano* **2011**, *5*, 2013−2019.

(9) Wang, G. P.; Zhang, L.; Zhang, J. J. A review of electrode materials for electrochemical supercapacitors. *Chem. Soc. Rev.* **2012**, *41*, 797−828.

(10) Brezesinski, T.; Wang, J.; Tolbert, S. H.; Dunn, B. Ordered Mesoporous R-MoO_3 with Iso-oriented Nanocrystalline Walls for Thin-Film Pseudocapacitors. *Nat. Mater.* **2010**, *9*, 146−151.

(11) El-Kady, M. F.; Strong, V.; Dubin, S.; Kaner, R. B. Laser scribing of high-performance and flexible graphene-based electrochemical capacitors. *Science* **2012**, *335*, 1326−1330.

(12) Sarkar, D.; Khan, G. G.; Singh, A. K.; Mandal, K. High-Performance Pseudocapacitor Electrodes Based on α-Fe_2O_3/MnO_2Core−Shell Nanowire Heterostructure Arrays. *J. Phys. Chem. C* **2013**, *117*, 15523−15531.

(13) Hakamada, M.; Moriguchi, A.; Mabuchi, M. Fabrication of carbon nanotube/$NiO_x(OH)_y$ nanocomposite by pulsed electrodeposition for supercapacitor applications. *J. Power Sources* **2014**, *245*, 324−330.

(14) Zhu, J.; Jiang, J.; Sun, Z.; Luo, J.; Fan, Z.; Huang, X.; Zhang, H.; Yu, T. 3D Carbon/Cobalt-Nickel Mixed-Oxide Hybrid Nanostructured Arrays for Asymmetric Supercapacitors. *Small* **2014**, *10*, 2937−2945.

(15) Chao, D.; Xia, X.; Zhu, C.; Wang, J.; Liu, J.; Lin, J.; Shen, Z.; Fan, H. J. Hollow nickel nanocorn arrays as three-dimensional and conductive support for metal oxides to boost supercapacitive performance. *Nanoscale* **2014**, *6*, 5691−5697.

(16) Singh, A. K.; Sarkar, D.; Khan, G. G.; Mandal, K. Hydrogenated NiO Nano-block Architecture for High Performance Pseudocapacitor. *ACS Appl. Mater. Interfaces* **2014**, *6*, 4684−4692.

(17) Wang, Y.; Zhang, Y.-Y.; Tang, J.; Wu, H.; Xu, M.; Peng, Z.; Gong, X.-G.; Zheng, G. Simultaneous Etching and Doping of TiO_2 Nanowire Arrays for Enhanced Photoelectrochemical Performance. *ACS Nano* **2013**, *7*, 9375−9383.

(18) Wang, X.; Zhu, H.; Xu, Y.; Wang, H.; Tao, Y.; Hark, S.; Xiao, X.; Li, Q. Aligned ZnO/CdTe Core Shell Nanocable Arrays on Indium Tin Oxide: Synthesis and Photoelectrochemical Properties. *ACS Nano* **2010**, *4*, 3302−3308.

(19) Zhu, A.; Zhao, Q.; Li, X.; Shi, Y. $BiFeO_3$/TiO_2 Nanotube Arrays Composite Electrode: Construction, Characterization, and Enhanced Photoelectrochemical Properties. *ACS Appl. Mater. Interfaces* **2014**, *6*, 671−679.

(20) Baker, D. R.; Kamat, P. V. Photosensitization of TiO_2 Nanostructures with CdS Quantum Dots: Particulate versus Tubular Support Architectures. *Adv. Funct. Mater.* **2009**, *19*, 805−811.

DOI: 10.1021/acssuschemeng.5b00519
ACS Sustainable Chem. Eng. 2015, 3, 2254−2263

(21) Leschkies, K. S.; Divakar, R.; Basu, J.; Enache-Pommer, E.; Boercker, J. E.; Carter, C. B.; Kortshagen, U. R.; Norris, D. J.; Aydil, E. S. Photosensitization of ZnO Nanowires with CdSe Quantum Dots for Photovoltaic Devices. *Nano Lett.* **2007**, *7*, 1793−1798.
(22) Luo, J.; Ma, L.; He, T.; Ng, C. F.; Wang, S.; Sun, H.; Fan, H. J. TiO_2/(CdS, CdSe, CdSeS) Nanorod Heterostructures and the Photoelectrochemical Properties. *J. Phys. Chem. C* **2012**, *116*, 11956−11963.
(23) Wang, Y.-G.; Wang, Z.-D.; Xia, Y.-Y. An asymmetric supercapacitor using RuO_2/TiO_2 nanotube composite and activated carbon electrodes. *Electrochim. Acta* **2005**, *50*, 5641−5646.
(24) Kim, J. H.; Zhu, K.; Yan, Y. F.; Perkins, C. L.; Frank, A. J. Microstructure and pseudocapacitive properties of electrodes constructed of oriented NiO-TiO_2 nanotube arrays. *Nano Lett.* **2010**, *10*, 4099−4104.
(25) Choi, T.; Lee, S.; Choi, Y. J.; Kiryukhin, V.; Cheong, S.-W. Switchable Ferroelectric Diode and Photovoltaic Effect in $BiFeO_3$. *Science* **2009**, *324*, 63−66.
(26) Yang, S. Y.; Seidel, J.; Byrnes, S. J.; Shafer, P.; Yang, C. H.; Rossell, M. D.; Yu, P.; Chu, Y. H.; Scott, J. F.; Ager, J. W. Above bandgap voltages from ferroelectric photovoltaic devices. *Nat. Nanotechnol.* **2010**, *5*, 143−147.
(27) Khan, G. G.; Das, R.; Mukherjee, N.; Mandal, K. Effect of metal-doping on highly efficient photovoltaics and switchable photovoltage in bismuth ferrite Nanotubes. *Phys. Status Solidi RRL* **2012**, *6*, 312−314.
(28) Das, R.; Khan, G. G.; Varma, S.; Mukherjee, G. D.; Mandal, K. Effect of Quantum Confinement on Optical and Magnetic Properties of Pr-Cr co-doped Bismuth Ferrite Nanowires. *J. Phys. Chem. C* **2013**, *117*, 20209−20216.
(29) Jaiswal, A.; Das, R.; Vivekanand, K.; Abraham, P. M.; Adyanthaya, S.; Poddar, P. Effect of reduced particle size on the magnetic properties of chemically synthesized $BiFeO_3$ nanocrystals. *J. Phys. Chem. C* **2010**, *114*, 2108−2115.
(30) Liu, H.; Yang, W.; Ma, Y.; Cao, Y.; Yao, J.; Zhang, J.; Hu, T. Synthesis and Characterization of Titania by Using a Photoassisited Sol-gel Method. *Langmuir* **2003**, *19*, 3001−3005.
(31) Sanjinés, R.; Tang, H.; Berger, H.; Gozzo, F.; Margaritondo, G.; Lévy, F. Electronic structure of anatase TiO_2 oxide. *J. Appl. Phys.* **1994**, *75*, 2945.
(32) Santara, B.; Giri, P. K.; Imakita, K.; Fujii, M. Evidence of oxygen vacancy induced room temperature ferromagnetism in solvothermally synthesized undopped TiO_2 nanoribbons. *Nanoscale* **2013**, *5*, 5476−5488.
(33) Luo, W. B.; Zhu, J.; Li, Y. R.; Wang, X. P.; Zhao, D.; Xiong, J.; Zhang, Y. *Appl. Phys. Lett.* **2007**, *91*, 082501.
(34) Eerenstein, W.; Morrison, F. D.; Dho, J.; Blamire, M. G.; Scott, J. F.; Mathur, N. D. Comment on "Epitaxial $BiFeO_3$Multiferroic Thin Film Heterostructures". *Science* **2005**, *307*, 1203.
(35) Zhang, F.; Hu, H.; Zhong, H.; Yan, N.; Chen, Q. Preparation of γ-Fe_2O_3@C@MoO_3 core/shell nanocomposites as magnetically recyclable catalysts for efficient and selective epoxidation of olefins. *Dalton Trans.* **2014**, *43*, 6041−6049.
(36) Chen, S.-W.; Lee, C.-C.; Chen, M.-T.; Wu, J.-M. Synthesis of $BiFeO_3$/ZnO core-shell heterostructures using ZnO nanorod positive templates. *Nanotechnology* **2011**, *22*, 115605.
(37) Lokhande, C. D.; Gujar, T. P.; Shinde, V. R.; Mane, R. S.; Han, S.-H. Electrochemical supercapacitor application of pervoskite thin films. *Electrochem. Commun.* **2007**, *9*, 1805−1809.
(38) Nithya, V. D.; KalaiSelvan, R.; Kalpana, D.; Vasylechko, L.; Sanjeeviraja, C. Synthesis of Bi_2WO_6 nanoparticles and its electrochemical properties in different electrolytes for pseudocapacitor electrodes. *Electrochim. Acta* **2013**, *109*, 720−731.
(39) Sarma, B.; Jurovitzki, A. L.; Smith, Y. R.; Mohanty, S. K.; Misra, M. Redox-induced Enhancement in Interfacial Capacitance of Titania Nanotube/Bismuth Oxide Composite Electrode. *ACS Appl. Mater. Interfaces* **2013**, *5*, 1688−1697.
(40) Vivier, V.; Régis, A.; Sagon, G.; Nedelec, J.-Y; Yu, L. T.; Cachet-Vivier, C. Cyclic voltammetry study of bismuth oxide Bi_2O_3 powder by means of a cavity microelectric coupled with Raman microspectrometry. *Electrochim. Acta* **2001**, *46*, 907−914.
(41) Wang, J.; Polleux, J.; Lim, J.; Dunn, B. Pseudocapacitive Contributions to Electrochemical Energy Storage in TiO_2 (Anatase) Nanoparticles. *J. Phys. Chem. C* **2007**, *111*, 14925−14931.
(42) Zhao, C.; Zheng, W.; Wang, X.; Zhang, H.; Cui, X.; Wang, H. Ultrahigh capacitive performance from both $Co(OH)_2$/graphene electrode and $K_3Fe(CN)_6$ electrolyte. *Sci. Rep.* **2013**, *3*, 2986−2991.
(43) Park, B.-O.; Lokhande, C. D.; Park, H.-S.; Jung, K.-D.; Joo, O.-S. Preparation of lead ruthenium oxide and its use in electrochemical capacitor. *Mater. Chem. Phys.* **2004**, *86*, 239−242.
(44) Cao, F.; Prakash, J. Performance investigations of $Pb_2Ru_2O_{6.5}$ oxide based pseudocapacitors. *J. Power Sources* **2001**, *92*, 40−44.
(45) Bang, H. J.; Lu, W.; Cao, F.; Prakash, J. An electrochemical double layer capacitor based on nanocrystalline lead ruthenatepyrochlore. *Electrochem. Commun.* **2000**, *2*, 653−657.
(46) Wholfahrt-Mehrens, M.; Schenk, J.; Wilde, P. M.; Abdelmula, E.; Axmann, P.; Garche, J. New materials for supercapacitors. *J. Power Sources* **2002**, *105*, 182−188.
(47) Pham, D. T.; Lee, T. H.; Luong, D. H.; Yao, F.; Ghosh, A.; Le, V. T.; Kim, T. H.; Li, B.; Chang, J.; Lee, Y. H. Carbon nanotube-bridged graphene 3D building blocks for ultrafast supercapacitors. *ACS Nano* **2015**, *9*, 2018−2027.
(48) Notarianni, M.; Liu, J.; Mirri, F.; Pasquali, M.; Motta, N. Graphene-based supercapacitor with carbon nanotube film as highly efficient current collector. *Nanotechnology* **2014**, *25*, 435405.
(49) Dong, X.-C.; Xu, H.; Wang, X.-W.; Huang, Y.-X.; Chan-Park, M. B.; Zhang, H.; Wang, L.-H.; Huang, W.; Chen, P. 3D Graphene Cobalt Oxide Electrode for High-Performance Supercapacitor and Enzymeless Glucose Detection. *ACS Nano* **2012**, *6*, 3206−3213.
(50) Luo, J. M.; Gao, B.; Zhang, X. G. High capacitive performance of nanostructured Mn−Ni−Co oxide composites for supercapacitor. *Mater. Res. Bull.* **2008**, *43*, 1119−1125.
(51) Jiao, Z.; Chen, T.; Xiong, J.; Wang, T.; Lu, G.; Ye, J.; Bi, Y. Visible-light-driven photoelectrochemical and photocatalytic performances of Cr-doped SrTiO3/TiO2 heterostructured nanotube arrays. *Sci. Rep.* **2013**, *3*, 2720.
(52) Wang, Y.; Zhang, Y.-Y.; Tang, J.; Wu, H.; Xu, M.; Peng, Z.; Gong, X.-G.; Zheng, G. Simultaneous Etching and Doping of TiO2 Nanowire Arrays for Enhanced Photoelectrochemical Performance. *ACS Nano* **2013**, *7*, 9375−9383.
(53) Wang, X.; Zhu, H.; Xu, Y.; Wang, H.; Tao, Y.; Hark, S.; Xiao, X.; Li, Q. Aligned ZnO/CdTe CoreShell Nanocable Arrays on Indium Tin Oxide: Synthesis and Photoelectrochemical Properties. *ACS Nano* **2010**, *4*, 3302−3308.
(54) Clark, S. J.; Robertson, J. Band gap and Schottky barrier heights of multiferroic $BiFeO_3$. *Appl. Phys. Lett.* **2007**, *90*, 132903.

DOI: 10.1021/acssuschemeng.5b00519
ACS Sustainable Chem. Eng. 2015, 3, 2254−2263